Inorganic Chemistry

Article

pubs.acs.org/IC

Spin Crossover Star-Shaped Metallomesogens of Iron(II)

Maksym Seredyuk,*[,†,&] M. Carmen Muñoz,[‡] Vadim Ksenofontov,[§] Philipp Gütlich,[§] Yury Galyametdinov,[∥] and Jose A. Real*[,†]

[†]Institut de Ciència Molecular (ICMol), Universitat de València, C/Catedrático José Beltrán Martínez, 2, 46980 Paterna (Valencia), Spain

[‡]Departament de Física Aplicada, Universitat Politècnica de València, Camino de Vera s/n, E-46022 Valencia, Spain

[§]Institut für Anorganische und Analytische Chemie, Johannes-Gutenberg-Universität, Staudinger-Weg 9, D-55099 Mainz, Germany

[∥]Kazan Physical Technical Institute, Russian Academy of Science, Sibirsky Tract 10/7, 420029 Kazan, Russia

Supporting Information

ABSTRACT: Three new types of spin crossover (SCO) metallomesogens of Fe^{II} based on symmetric tripod ligands and their magnetic and structural properties are reported here. These were obtained by condensation of tris(2-aminoethyl)-amin (tren) with the aldehyde derived from 3-alkoxy-6-methylpyridine (**mpyN**, N (number of carbon atoms in *n*-alkyl chains) = 8, 18), 1-alkyl-1*H*-imidazole (**imN**, N = 4, 16, 18, 20, 22), or 1-alkyl-1*H*-benzimidazole (**bimN**, N = 6, 14, 16, 18, 20). A complex derived from 1-octadecyl-1*H*-naphtho[2,3-*d*]imidazole (**nim18**) retains the high spin state at any temperature. Single crystals of the short-chain complexes were investigated by a combination of X-ray crystallography, magnetic measurements and Mössbauer spectroscopy. Generally, in comparison with the short-chain complexes the long-chain complexes display more gradual SCO and undergo a phase transition crystal−liquid crystal that is reflected in their magnetic properties. Characterization by X-ray powder diffractometry and differential calorimetry reveal formation of a smectic mesophase upon melting.

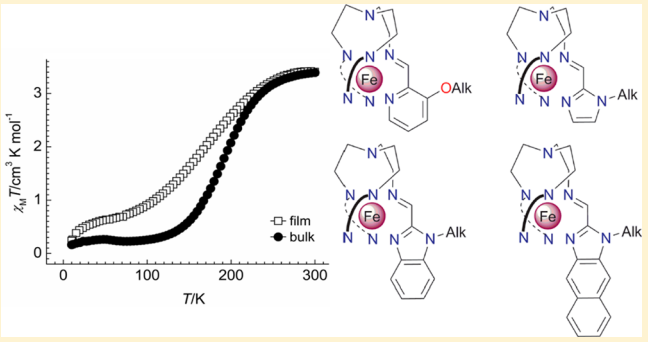

INTRODUCTION

The spin crossover (SCO) phenomenon observed in transition metal complexes with electronic configurations $3d^{4-7}$ represents one of the best examples of molecular bistability in coordination chemistry. Since the discovery in tris(dithiocarbamato) complexes of Fe^{III},[1] the study of the SCO has evolved to a mature research field where, aside from academic interest, exists a potential of applications for these materials in devices of technological interest such as memory elements,[2a] displays,[2b] electric field switchable devices.[3]

Through a perturbation by temperature, light, or pressure[4] the SCO molecules can be reversibly switched between the low-spin (LS) state and the high-spin (HS) state with corresponding variation of magnetic, dielectric, and optical responses.[4,5] The SCO phenomenon can be described as an intraionic electron transfer between the t_{2g} and e_g orbitals strongly coupled with significant structural changes, primarily metal-to-ligand bond lengths and angles leading to a modification of the molecular volume and consequently the lattice parameters and the cell volume of the crystal.[6] Thus, the spin-state change is consubstantial with a structural phase transition (PT). Furthermore, additional *extrinsic* PTs may influence the SCO behavior of the compound. However, rather rarely are extrinsic PTs synchronized with the change of the spin state or are its driving factor. Thus, only a limited number of SCO events have been clearly demonstrated to be coupled with extrinsic PTs.[7] In general, the appearance of extrinsic PTs is rather unpredictable and usually associated with subtle structural changes, which often produce different molecular isomers and/or different packing patterns of structurally equivalent molecules in the crystal lattice giving polymorphs, which strikingly influence the SCO properties.[8] In this regard, soft molecular materials made up of metal complexes functionalized with long alkyl substituents (metallomesogens) are particularly well suited because of their ability to melt.[9] The controllable melting temperature of metallomesogens encouraged us to investigate the properties of Fe^{II} complexes exhibiting crystal−liquid crystal PT and the SCO phenomenon.[10] This led to the first documented case of SCO behavior driven by structural changes associated with a crystal−smectic A transition.[10c] Furthermore, a reversible modification of the SCO due to a transition to the liquid crystalline state as well as a clear dependence of the transition temperature on the number of carbon atoms of the alkyl substituents was described for another series of Fe^{II} SCO metallomesogens.[10d] In both cases it was found that the melting is the reason for a modification of the structure leading to a change of the ligand

Received: May 6, 2014
Published: August 1, 2014

   dx.doi.org/10.1021/ic5010159 | *Inorg. Chem.* 2014, 53, 8442−8454

field strength and cooperative interactions between SCO centers.[11] On the basis of the performed studies, a classification of SCO metallomesogens on the type of interaction was proposed:[11] type *i* systems with coupled phase transitions, subdivided into three groups *a*, *b*, and *c* (in *a* the structural changes associated with the Cr↔LC drive the SCO, while in *b* these structural changes influence the spin state but they are not the driving force of the SCO; *c* concerns the systems where the glass transition of the material inhibits the SCO properties); type *ii*: systems where both transitions coexist in the same temperature region but are not coupled due to competition with the dehydration; type *iii*: systems where both transitions are uncoupled, subdivided into groups *a* and *b* (in *a* the both occur in different temperature regions, in *b* despite overlap of both, the magnetic properties remain unaffected[10g]).

The motivation for this work arose from a need to understand more deeply structure–properties relationships and factors responsible for efficient control of the SCO process by a phase transition, particularly, the factors governing the strength (extent) of the influence of a phase transition on SCO. Therefore, as a part of our continuing interest in the study of Fe^{II} SCO metallomesogens, we have systematically exploited a new type of star-shaped Fe^{II} SCO complex based on symmetric tripod ligands, obtained by condensation of tris(2-aminoethyl)-amin (tren) and alkylated heterocyclic aldehydes. The choice of the ligands for the present study is based on the convenient combination of synthetic accessibility of alkylated derivatives and the right range of field strength to observe SCO in the region near to the ambient temperature where the phase transition, solid–liquid crystal, takes place.

The goals of the studies reported here are to check the influence of the new geometry of the complexes on the SCO and mesogenic properties, to analyze the structure of metallomesogens and the structural changes upon melting, and to give reasonable explanation of the observed interplay with the SCO. Also, we wanted to demonstrate the processability of the Fe^{II} metallomesogens, particularly for the preparation of thin films by the spin-coating method.

To describe the systems, the nomenclature **xN** was adopted, where **x** represents the type of the pendant substituents of a tripod ligand together with the utilized anion, which are 3-alkoxy-6-methylpyridine and BF_4^- (**mpyN**), 1-alkyl-1*H*-imidazole and BF_4^- (**imN**), 1-alkyl-1*H*-benzimidazole and ClO_4^- (**bimN**) and, finally, 1-alkyl-1*H*-naphtho[2,3-*d*]imidazole and ClO_4^- (**nimN**); **N** corresponds to the number of atoms in *n*-alkyl chains, Alk (Scheme 1).

Magnetic Susceptibility Measurements. The thermal dependence of the product $\chi_M T$ vs T (χ_M being the molar susceptibility and T the temperature) for short-chain **mpy8**·0.5H_2O, **im4**·MeOH, and **bim6** as well as for representative long-chain **mpy18**, **im18**, **bim18**, and **nim18** are shown in Figures 1–3 together with the HS molar fraction, γ_{HS}, obtained from Mössbauer spectra at representative temperatures (see Supporting Information [SI] Figures S1 and S2 and Table S1). The plots of the remaining compounds are shown in the SI, Figure S3.

At temperatures below 100 K, **mpy8**·0.5H_2O shows values of $\chi_M T \approx 1.6$ cm^3 K mol^{-1} indicating the presence of a paramagnetic residue (~50%) of Fe^{II} ions in the HS state (Figure 1a). Upon heating, **mpy8**·0.5H_2O undergoes a gradual SCO transition with a change of slope at 180 K whereas upon further heating the $\chi_M T$ value increases up to ~3.4 cm^3 K mol^{-1}. Upon subsequent cooling the magnetic behavior does not match the first heating curve, suggesting dehydration of the sample confirmed by thermogravimetric (TGA) data (Figure S4 in the SI). The magnetic data of the resulting compound **mpy8** show a hysteresis of the SCO with $T_{1/2}^{\uparrow}$ = 155 K and $T_{1/2}^{\downarrow}$ = 144 K ($T_{1/2}$ is the temperature at which the molar fraction for LS and HS is equal to 50%). Upon irradiation of **mpy8** with green light (532 nm) over 3 h at 10 K a photostationary regime can be attained (LIESST effect[12]) with the percentage of photoconverted HS state equal to ~50% as inferred from the maximum of $\chi_M T$ value at 25 K. The relaxation temperature of the HS metastable state (T_{LIESST}[12b]) was found to be 53 K.

Scheme 1. Schematic Structure of Studied Complexes

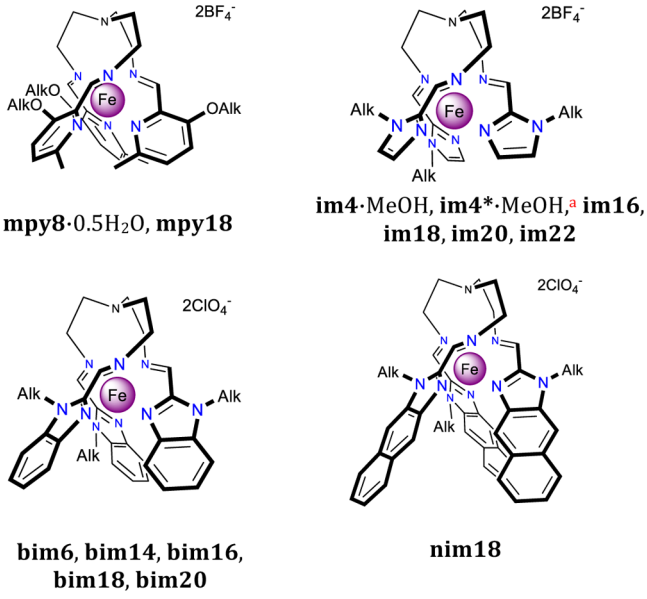

[a] has ClO_4^- instead of BF_4^-

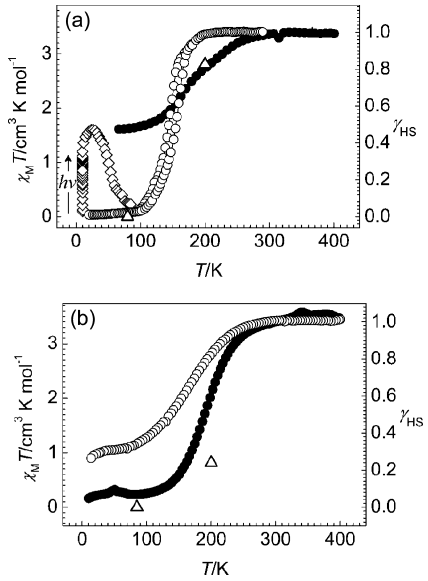

Figure 1. Thermal variation of the $\chi_M T$ vs T for: (a) nonheated **mpy8**·0.5H_2O (●) and dehydrated form **mpy8** (○). Symbol Δ corresponds to Mössbauer data of **mpy8**; (b) Magnetic data for **mpy18** before (●) and after thermal treatment (○); Symbol Δ corresponds to Mössbauer data of the nonheated sample.

dx.doi.org/10.1021/ic5010159 | Inorg. Chem. 2014, 53, 8442–8454

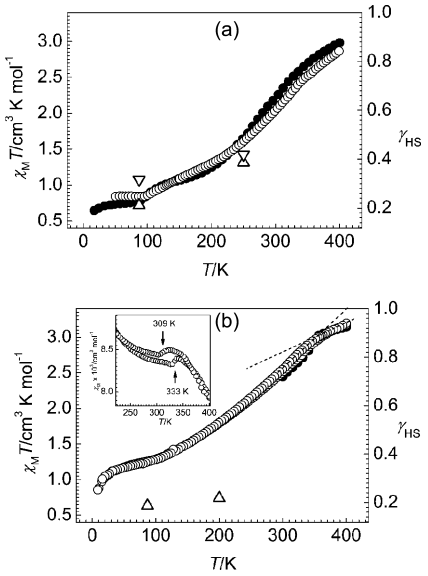

Figure 2. Magnetic data for: (a) **im4**·MeOH (●) and **im4***·MeOH (○); Symbol Δ corresponds to Mössbauer data of **im4**·MeOH and symbol ∇ to **im4***·MeOH; (b) **im18** before (●) and after heating (○). Symbol Δ corresponds to Mössbauer data of the nonheated sample. The dashed lines show change of the slope of the magnetic curve after melting.

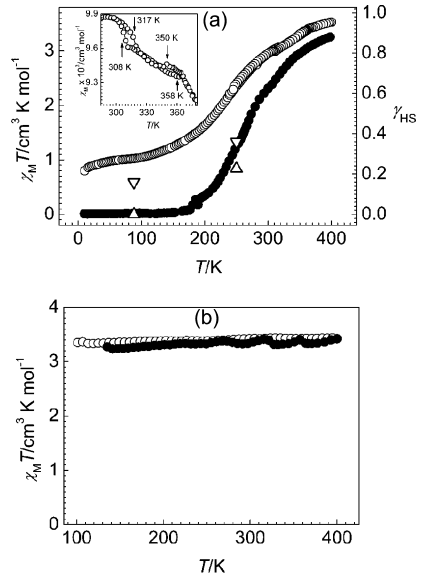

Figure 3. (a) Magnetic data for **bim6** (●) and **bim18** (○). Inset shows hysteresis loops for **bim18**. Symbol Δ corresponds to Mössbauer data of **bim6** and symbol ∇ – to **bim18**; (b) Magnetic data for **nim18** before (●) and after heating (○).

The nonheated **mpy18** exhibits complete SCO centered at $T_{1/2}$ = 192 K. However, after thermal treatment the SCO becomes less complete, and consequently $T_{1/2}$ shifts down to 166 K (Figure 1b). These results deserve to be compared with those of the analogous compound **A18**, derivative of 5-alkoxypyridine (Scheme 2). The latter showed a complete SCO almost insensitive to the thermal treatment centered at 133 K.[10c,13]

The compounds **im4** and **im18** exhibit a gradual SCO in the temperature range 100–400 K with extreme $\chi_M T$ in the interval 0.7–3.0 cm^3 K mol^{-1} (Figure 2a, b). It is worth stressing that the magnetic behavior of the long alkylated chain compound **im18** follows a melting PT taking place at ~320 K. The heating and cooling experiments reveal reversible divergence for ascending and descending magnetic curves with critical temperatures $T^{\downarrow}$ = 309 K and $T^{\uparrow}$ = 333 K, respectively, defining a small hysteresis loop clearly seen in the χ_M versus T plot (see inset of Figure 2b). In addition, a change of slope is observed in the $\chi_M T$ versus T plot at the same temperature where the crystal-to-liquid crystal PT takes place (vide infra). The magnetic behavior of **imN**, N = 16, 20, 22 is very similar to that of **im18** (see Figure S3).

The short-chain compound **bim6** is diamagnetic up to 180 K, while above this temperature it undergoes a thermally driven SCO centered at 280 K and at 400 K reaches $\chi_M T$ = 3.3 cm^3 K mol^{-1} (Figure 3a). The long-chain congener **bim18** shows incomplete SCO transition at low temperature and gradual SCO upon heating, whereas heating and cooling curves diverge in the points of two consequent PTs with critical parameters $T_1^{\uparrow}$ = 317 K and $T_1^{\downarrow}$ = 308 K and $T_2^{\uparrow}$ = 358 and $T_2^{\downarrow}$ = 350 K (Figure 3a, inset in coordinates χ_M vs T).

Compound **nim18** is HS in the temperature region 100–400 K in heating and cooling modes (Figure 3b).

Crystal and Molecular Structure of mpy8·0.5H$_2$O, im4*·MeOH, and bim6. At 120 and 250 K, **mpy8**·0.5H$_2$O displays the triclinic space group $P\bar{1}$, whereas **im4***·MeOH and **bim6** adopt the trigonal $R\bar{3}$ and the monoclinic $P21/c$ space groups, respectively. Selected crystallographic data, bond distances, and distortion parameters θ and Σ^{7k} are given in Tables 1–4. The iron atoms adopt a pseudo-octahedral symmetry and are surrounded by six nitrogen atoms belonging to three imino groups and three heterocycles of the corresponding trifurcated ligands.

The unit cell of **mpy8**·0.5H$_2$O contains two pairs of independent complex molecules with opposite chirality and eight BF_4^- anions compensating the charge (Z = 2) (Figure 4a). At 120 K, one of the two molecules remains in HS state as evidenced by averaged bond length Fe–N, 2.238(5) Å, and typical for this type of compounds contact distance Fe···N^{tert} to the tertiary apical nitrogen which depends on the spin state of the Fe^{II} ion,[6,14] is 3.069(5) Å. Distortion parameters of octahedron θ and Σ are equal to 8.456° and 116.55(18)°, respectively. The second complex molecule is in LS state with corresponding parameters 2.020(5) Å, 3.563(5) Å, 4.777° and 77.53(18)°, serially. Upon increase of temperature, this second complex molecule undergoes thermally induced SCO as follows from increased values of the structural parameters being now 2.234(5) Å, 3.048(5) Å, 8.067°, 106.02(18)° serially; thus, both independent complex molecules are HS at 200 K. The modifications of the coordination sphere of **mpy8** due to SCO are directly reflected of the form of the SCO complex molecule, which is illustrated by the distinguishable divergence of the overlaid HS and LS structures (Figure S5 in the SI).

The presence of alkyl chains tethered to pyridine rings in **mpy8**·0.5H$_2$O results in a structure reflecting the incompatibility of packing preferences of the lipophilic alkyl chains, on one hand, and cationic head groups of the complex molecules and anions, on the other hand. Radially protruding alkyl substituents do not participate in ionic interactions of charged counterparts and are expelled out of ionic layers. Consequently, stacking of these layers in the lattice gives packing with alternating ionic and alkyl layers with periodicity of ~15.6 Å at 120 K and ~16.0 Å at 200 K (Figure 5a).

dx.doi.org/10.1021/ic5010159 | Inorg. Chem. 2014, 53, 8442–8454

Scheme 2. Schematic Structure of Related SCO Metallomesogens of Fe^{II}

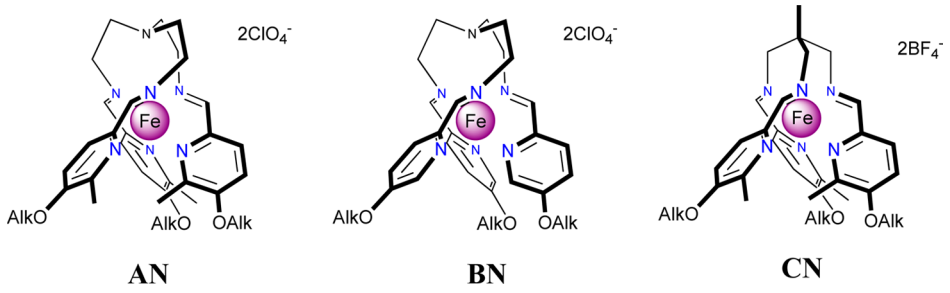

Table 1. Crystallographic Data for mpy8·0.5H_2O, im4*·MeOH, and bim6

	mpy8·0.5H_2O		im4*·MeOH		bim6	
empirical formula	$C_{102}H_{164}B_4F_{16}Fe_2N_{14}O_7$		$C_{30}H_{48}Cl_2FeN_{10}O_8$		$C_{48}H_{66}Cl_2FeN_{10}O_8$	
M_r [g mol^{-1}]	2157.41		803.53		1037.86	
crystal system	triclinic		trigonal		monoclinic	
space group	$P\bar{1}$		$R\bar{3}$		$P2_1/c$	
Z	2		18		4	
T [K]	120	200	120	250	120	298
a [Å]	16.229(5)	16.659(5)	17.960(1)	18.114(1)	15.760(2)	16.055(1)
b [Å]	19.229(5)	19.282(5)			13.638(1)	13.846(1)
c [Å]	20.049(5)	20.092(5)	62.813(1)	63.651(1)	24.499(3)	24.783(1)
α [deg]	64.687(5)	65.247(5)	90	90	90	90
β [deg]	75.385(5)	76.038(5)	90	90	103.348(13)	102.235(6)
γ [deg]	78.892(5)	76.846(5)	120	120	90	90
V [$Å^3$]	5447(3)	5629 (3)	17547.3(7)	18087.5(7)	5123.5(10)	5384.0(5)
ρ_{calcd} [mg m^{-3}]	1.315	1.273	1.369	1.328	1.345	1.280
μ [mm^{-1}]	0.35	0.34	0.58	0.56	0.46	0.44
$R1[I > 2\sigma(I)]$	0.0773	0.0730	0.0351	0.0502	0.0501	0.0844
$wR2$	0.0967	0.0886	0.0470	0.0833	0.0672	0.0976

Table 2. Bond Distances Fe−N and Distortion Parameters θ and Σ for mpy8

	120 K			200 K		
	Fe1	Fe2	averaged	Fe1	Fe2	averaged
<Fe−N>	2.020(5)	2.238(5)	2.129(5)	2.234(5)	2.239(5)	2.237(5)
θ [deg]	4.777	8.456	6.616	8.067	8.461	8.264
Σ [deg]	77.53(18)	116.55(18)	97.04(18)	106.02(18)	113.70(18)	109.86(18)
<Fe···N^{tert}> [Å]	3.563(5)	3.069(5)	3.316(5)	3.048(5)	3.207(5)	3.128(5)

Table 3. Bond Distances Fe−N and Distortion Parameters θ and Σ for bim6

	120 K	250 K
<Fe−N > [Å]	1.978(6)	2.112(6)
θ [deg]	5.122	7.135
Σ [deg]	63.2 (2)	79.6 (2)
<Fe···N^{tert}> [Å]	3.441(8)	3.121(5)

Essentially, the ionic layers are monolayers where each constituting complex molecule provides alkyl chains on both sides of the layer. The alkyl chains are distorted by *gauche* conformations of methylene groups and do not form a regular aliphatic sublattice unlike that observed for related compounds **A6**[10c] and **B12**,[10g] derivatives of 5-alkoxypyridine (Scheme 2). The crystal packing of cationic heads of the last two compounds is not perturbed by alkyl chains and is very similar to that of the parent unsubstituted compound {Fe[tren-$(PyMe)_3$]}$(ClO_4)_2$,[6] whereas in **mpy8** the packing motif is completely different. Also, in the related **A6** the weak hydrogen-bonding network has a two-dimensional character and spreads within the ionic layers, while in **mpy8** all weak hydrogen CH···F(B) contacts [2.274(5)−2.659(5) Å at 120 K, 2.246(5)−2.657(5) Å at 200 K] belong to three-dimensional inter- and intralayer hydrogen-bonding networks. Additionally, there are contacts element to element between carbon atoms of the ligand skeleton with fluorine atoms of anions or crystal water molecule with length distances lying in the range of 2.775(5)−3.654(5) Å at 120 K and 3.090(5)−3.165(5) Å at 200 K. No $\pi-\pi$ stacking interactions are observed similarly to the compound **A6**.[10c]

The crystal structure of **bim6** is comparable to that of **mpy8**. First of all, in **bim6** each cell contains two pairs of complex molecules of opposite chirality and eight disordered ClO_4^- anions balancing the charge (Figure 4b). At 120 K the complex molecule exhibits an average Fe−N bond length equal to 1.978(6) Å. The distance between the tertiary nitrogen atom N7 and iron(II) ion of 3.441(8) Å and both distortion parameters θ and Σ equal 5.122° and 63.2 (2)°, respectively, are obviously indicative of the LS state of the central atom. Heating up to 298 K changes these parameters to 2.112(6) Å, 3.121(5) Å, 7.135°, 79.6 (2)°, serially, reflecting a partial

dx.doi.org/10.1021/ic5010159 | Inorg. Chem. 2014, 53, 8442−8454

Table 4. Bond Distances Fe−N and Distortion Parameters θ and Σ for im4*·MeOH

	Fe1	Fe2	Fe3	averaged
		120 K		
<Fe−*N* > [Å]	1.981(3)	1.970(3)	2.127(3)	2.026(3)
θ [deg]	5.689	5.044	8.015	6.249
Σ [deg]	58.38 (11)	67.14 (11)	95.70 (11)	73.74 (11)
<Fe···N^{tert}> [Å]	3.360 (6)	3.347 (6)	2.941(6)	3.220 (6)
		250 K		
<Fe−*N* > [Å]	2.063(3)	1.981(3)	2.162(3)	2.069(4)
θ [deg]	7.011	5.093	8.714	6.939
Σ [deg]	77.58 (12)	65.53 (12)	106.17 (12)	83.09 (12)
<Fe···N^{tert}> [Å]	3.116 (7)	3.320 (6)	2.863 (6)	3.100 (6)

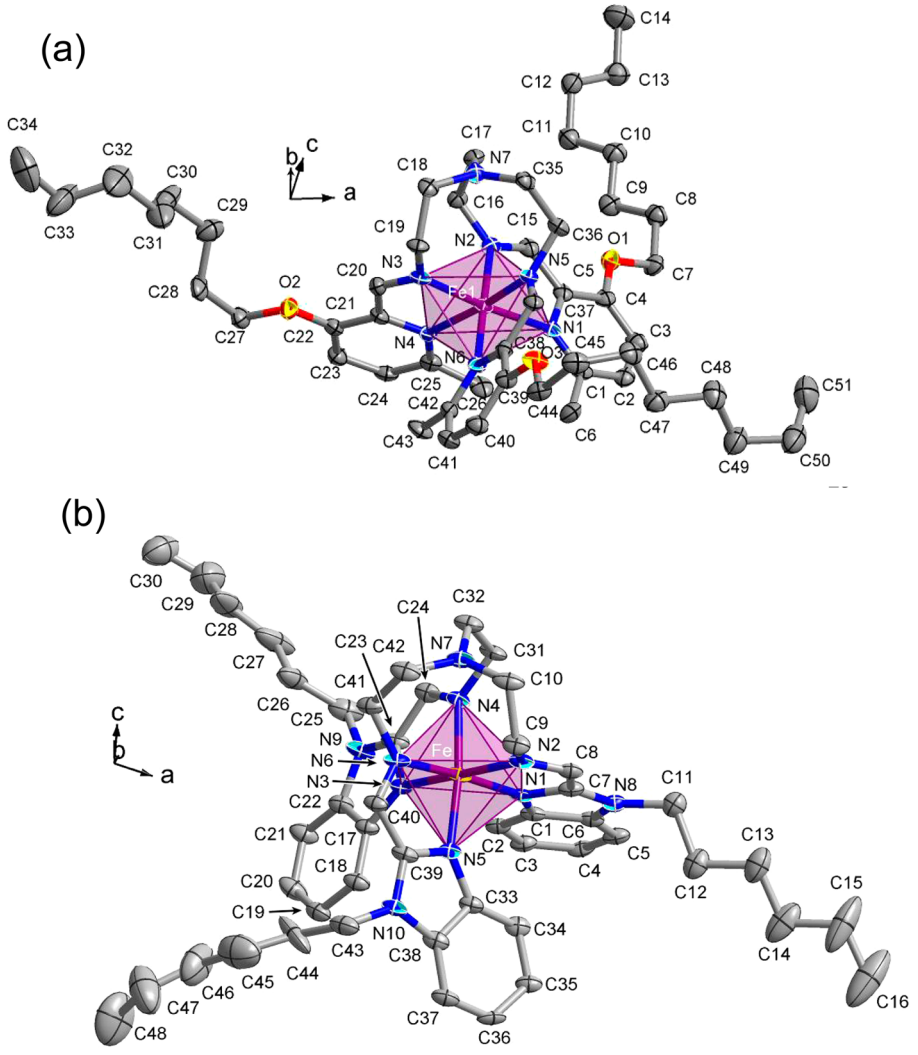

Figure 4. Mononuclear cationic complexes $[FeL]^{2+}$ in the crystal structures of **mpy8** (a) and **bim6** (b). Thermal ellipsoids at 50% probability level.

transformation to the HS state at this temperature. Indeed, the difference between the bond lengths at both temperatures is 0.137 Å, and taking into account that the difference in the average Fe−N bond length between the LS and HS states is typically 0.2 Å, a percentage of Fe^{II} centers in the HS state of 68% is found, a value which is consistent with the magnetic data.

In the crystal packing of **bim6**, the formed lamellar structure has periodicity of ∼15.3 Å at 120 K and 15.7 Å at 298 K and is composed of repeating monomolecular ionic layers of headgroups and anions, and with alkyl chains filling the interlayer space (Figure 5b). As in the case of **mpy8**, the distance between the alkyl chains is too large, and their length is insufficient to form a well-ordered aliphatic sublattice despite the fact that all methylene groups are in the stretched *all-trans* conformation. The observed CH···O(Cl) contacts are in the range of 2.205(5)−2.718(5) Å at 120 K and change little to 2.258(5)−2.709(5) Å at 298 K. There are pairs formed by

dx.doi.org/10.1021/ic5010159 | *Inorg. Chem.* 2014, 53, 8442−8454

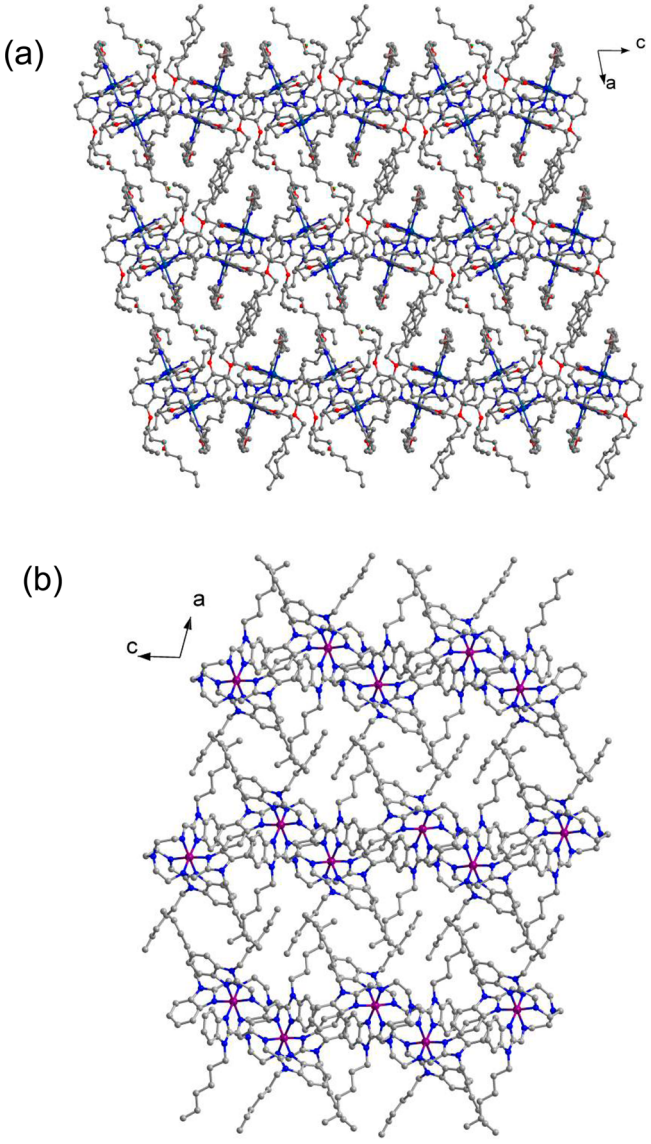

Figure 5. Crystal packing of **mpy8**·0.5H_2O (a) and **bim6** (b) showing arrangement with alternating ionic layers and alkyl chains. Anions are omitted for clarity.

neighboring complex molecules of opposite chirality which are connected by a $\pi-\pi$ stacking interaction between benzimidazole groups with an interplane distance of 3.321(5) Å at low temperature changing to 3.572(5) Å in the high-temperature structure.

Attempts to obtain good-quality crystals of **im4**·MeOH (with BF_4^- as counteranion) failed; therefore, the structural characterization of isomorphous **im4***·MeOH (has ClO_4^- counteranion) (see XRPDs in Figure S6 in the SI) is given below. The crystal structure of **im4***·MeOH adopts the trigonal space group $R\bar{3}$ with a cell containing eighteen complex molecules together with thirty-six ClO_4^- anions (Figure 6a). One out of three independent complex molecules undergoes partial transition to the HS state upon heating from 120 up to 250 K (<Fe1−*N*> is 1.981(3) and 2.063(3) Å, respectively), while the second complex molecule remains in LS state upon heating as evidenced by almost nonchanging <Fe2−*N*> distance (1.970(3) and 1.981(3) Å, respectively). The third complex molecule is partially HS at 120 K and displays further increase of distance <Fe3−*N*> at the higher temperature (from 2.127(3) to 2.162(3) Å, respectively). The change of the Fe···N^{tert} contact distance and the distortion parameters θ and Σ in each complex molecule are in line with spin-state change of the central atoms (see Table 4).

The three independent complex molecules unite in a supramolecular aggregate with collinear iron atoms {Fe1···Fe3···Fe2} which repeats by an inversion symmetry operation infinitely along *c*, forming a columnar superstructure (at 120 K, distances Fe3···Fe1 and Fe3···Fe2 are 10.372(3) Å and 9.252(3) Å, respectively, and at 250 K are 10.388(3) and 9.435(3) Å, respectively). Coordination heads constituting the inner part of the columns are surrounded by alkyl substituents together with anions participating in the formation of weak hydrogen bonds with distances CH···O(Cl) lying in the range 2.470(3)−2.715(3) at 120 K and 2.321(3)−2.702(3) Å at 250 K.

The columns of the complex molecules are not uniform, but there are voids due to loosely connected aggregates {Fe1···Fe3···Fe2} with Fe1···Fe1$^{\#}$ distance being 16.375(1) Å at 120 K and 16.683(1) Å at 250 K (#: 0.667−*x*, 1.333−*y*, 0.333−*z*). Further, each void, encaging six hydrogen-bonded molecules of methanol, is surrounded by six complex molecules of neighboring columns; in total eight complex molecules and six ClO_4^- anions decorate the formed cavity (V = 492 Å^3 at 120 K and 506 Å^3 at 250 K[15]). Due to screw axes of the third order, the cavities of neighboring columns are shifted from each other by the distance *c*/3 and therefore are isolated (Figure S7 in the SI).

XRD and DSC study of mpy18, imN, bimN, and nim18. The title compounds belong to the family of tris(α-diimine) Fe^{II} complexes, characterized by intense coloration due to symmetry-allowed charge-transfer band.[16] This fact together with the strong tendency to homeotropic alignment of the ionic metallomesogens prevents phase identification by polarizing optical microscopy (POM). However, POM studies confirm the liquid-like nature for **mpy18**, **im18**, **bim18**, and **nim18** which are resistant to shear at lower temperatures in crystalline phases, but flow at higher temperatures in mesophases. Alternatively, X-ray diffraction (XRD) at different temperatures is an appropriate technique to further characterize these materials. Here below we will discuss the XRD of the representative compounds **mpy18**, **im18**, **bim18**, and **nim18**.

The four types of long-chain complexes manifest lamellar structure in the crystalline state as evidenced by the powder XRD patterns at 300 K, rendering an intense low angle peak together with the weaker ones with *d*-spacing 1:1/2:1/3:1/4 (Figure 7). The other observed peaks are smaller in intensity that is characteristic for long alkyl-chain materials because of the high degree of preferred orientation. The interlayer distance *d* at different temperatures calculated from the Bragg's equation is summarized in Table 5.

Upon heating, the crystallinity of the compounds normally decreases;[17] this is clearly observed for **mpy18** and **bim18** (Figure 7a,c) and especially pronounced for **imN** series where heating up to 400 K is accompanied by attenuation of the lamellar diffractions. After cooling back to the crystalline state, at 300 K the samples of **imN**, N = 18, 20, 22, display partial recovery of the weaker diffraction (20) (Figure S8 in the SI). It is worth noting, that the weaker the peak (20) with respect to the (10) one, the more disordered the layers are.[17a] For **bimN** and **nim18** to a lesser extent, the melting changes the character of the observed diffraction patterns and the presence of minor

dx.doi.org/10.1021/ic5010159 | *Inorg. Chem.* 2014, 53, 8442−8454

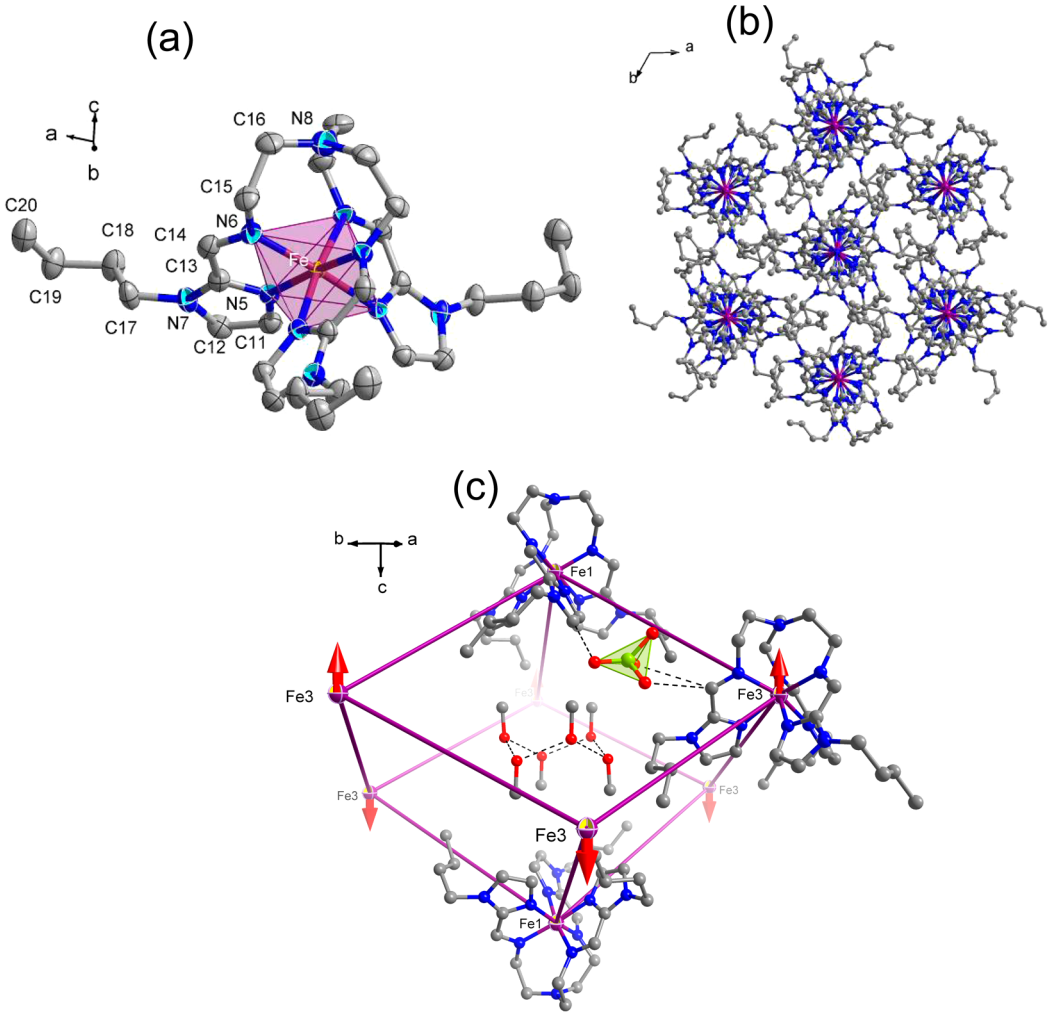

Figure 6. Mononuclear cationic complexes $[FeL]^{2+}$ in the crystal structures of **im4***·MeOH (b) Projection of the crystal packing of **im4***·MeOH along *c* (a). (b) A cavity with caged methanol molecules decorated by complex cations and anions. Arrows show orientation of Fe3-complex molecules.

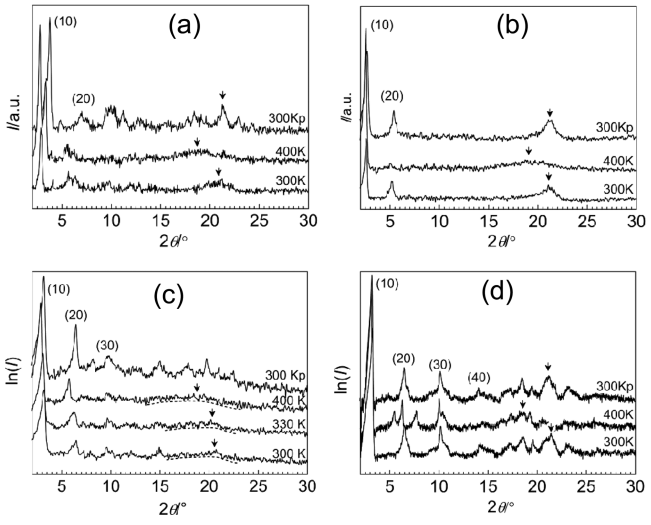

Figure 7. Diffractograms for **mpy18** (a), **im18** (b), **bim18** (c), and **nim18** (d) at indicated temperatures; p corresponds to nonheated sample. Arrows show maxima of alkyl halo. Note, because of low intensity of diffraction peaks, plots (c) and (d) are presented in coordinates ln(*I*) vs 2*θ*.

diffractions. On the other hand, despite a relatively high crystallinity of these samples, the poor resolution of the peaks and their low intensity does not allow reliable indexing of all observed peaks in the XRD profiles.

There is a clear increase in the number of minor peaks in the diffractograms when moving from **im18** to **bim18** and then to **nim18**. This observation indicates that with the increasing size of cationic head-groups of the complexes the mesophases possess a greater degree of crystalline order. The observed low intensity of alkyl halo at $2\theta = 19-21^\circ$ we attribute to a badly organized aliphatic sublattice due to the large distance between alkyl chains bound to the voluminous head-groups.

From this analysis of the XRD profiles, it can be suggested that the structure of the long-chain compounds is to some extent similar to the crystal structure of the above-described short-chain homologues **mpy8** and **bim6**. Accordingly, coordination head-groups and anions in **mpy18**, **imN**, **bimN**, and **nim18** are arranged in ionic monolayers in a way that each molecule supplies one and two alkyl chains on each side of the formed monolayer, whereas alkyl chains of neighboring layers intertwine. The last statement follows from the comparison of the full length of, for example, **im18** in the stretched configuration, ∼50 Å (Figure S9 in the SI), and *d* spacing between neighboring layers determined from XRD data, 33.5 Å.

dx.doi.org/10.1021/ic5010159 | *Inorg. Chem.* 2014, 53, 8442−8454

Table 5. Interlayer Distances *d* at Different Temperatures, Thermal Transitions and Mesomorphism, Enthalpy ΔH^{PT} and entropy ΔS^{PT} of Phase Transition and Thermal Stability Determined by XRD, DSC, and TGA for Indicated Compounds

	d/Å					
cmpd	300 K nonheated	400 K	300 K	thermal transitions/K[a]	ΔH^{PT}/kJ mol^{-1}[a]	ΔS^{PT}/J K^{-1} mol^{-1}
mpy18	24.1	32.1, 26.5	30.6	Cr 330/320[b] S_X 450[c] D	43.2	130.9
im18	33.5	34.6	34.2	Cr 328/312 S_X 509 D	83.9	262.2
bim18	27.3	30.5	27.7	Cr1 316/313 Cr_2 357/347 S_X 463 D	25.4, 48.1	136.6
nim18	27.3	28.1	27.2	Cr 310/306 S_X 478 D	12.7	41.3

[a]Measured by the DSC on the second heating−cooling cycle. The values correspond to the maxima of the enthalpy peaks. The identification of the mesophase was done on the basis of the XRD data. Cr, crystalline; S_X, smectic X; D, decomposition. [b]Transition temperature upon heating/cooling. [c]Onset of the decomposition according to the TGA data.

Detailed analysis of the interlayer distance at different temperatures in homologous series given in the SI (Figure S10 and Table S2) leads to the conclusion about longitudinal changes at the level of the coordination head-groups, i.e. some reorganization of the ionic monolayers occurs upon melting.

The phase transitions of compounds with N = 18 were investigated using differential scanning calorimetry (DSC) (Figure 8). The first heating run for these compounds does not coincide with the second one as expected from the structure annealing monitored by the XRD technique upon heating and mismatch of the first heating magnetic curve with subsequent ones. During the first cooling and the second heating run, heat capacity anomalies located above 300 K correspond to the PT observed in these compounds. For all compounds the melting of annealed samples takes place in two steps, as follows from the presence of double peaks (**mpy18**, **bim18**, **nim18**) or a peak with a shoulder (**im18**) in the corresponding profiles. Solid−solid and order−disorder pretransitions[18] are known to be observed for similar compounds.[10c,d,g] The melting of long alkyl chains in metallomesogens even with a simple molecular structure, such as, for example, *n*-alkylammonium metalates and metal carboxylates, is often a complicated process producing intermediate phases before melting.[19] In this respect, the occurrence of multiple transitions is a remarkable effect observed for **bim18** where separation between two strong thermal peaks reaches 41 K ($T_1^{\uparrow}$ = 316 K and $T_2^{\uparrow}$ = 357 K; Figure 8c). These two transitions are the sources of discontinuities on the magnetic curve, but differ from the viewpoint of the structural transformation as can be elucidated from the XRD profiles of **bim18** at 400 and 330 K (Figure 7c). Namely, at 330 K the alkyl halo at 2θ = 19−21° is solid-like, similarly to that at 300 K; however, at 400 K it becomes broader and shifts to lower 2θ values typical for the liquid-like state. Accounting for this, the intermediate phase was labeled as the second crystalline phase Cr_2, while the phase at the higher temperature corresponds to the mesophase S_X.

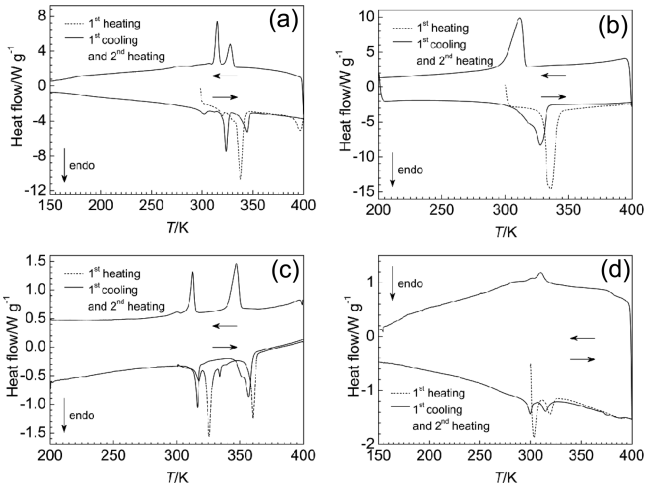

Figure 8. DSC traces for: **mpy18** (a), **im18** (b), **bim18** (c), and **nim18** (d) in the heating and cooling mode at 10 K/min.

An attenuation of structural changes upon melting follows from the XRD data for the series **im18**, **bim18**, **nim18**. In the same order the heat flow upon melting decreases as follows from the calorimetric data. The largest value of ΔH^{PT} is observed for **im18** (83.9 kJ mol^{-1}), somewhat lower for **bim18** (total heat effect of two transitions is 73.5 kJ mol^{-1}), and the lowest for **nim18** (12.7 kJ mol^{-1}). It was shown earlier that the heat flow upon heating combines enthalpy gain from the transition of ordered alkyl chains to the quasi-liquid disordered state and the heat effect of the concomitant perturbation of ionic layers.[17a,20] On the basis of this and also on the XRD data a conclusion can be made that, due to the increasing size of the head-groups in the series **im18**, **bim18**, **nim18** and the increasing degree of intermolecular interactions ($\pi-\pi$ stacking, weak hydrogen bonds), the degree of the ordering of monolayers increases, and they become more robust toward perturbations imposed by alkyl chains undergoing transformations upon heating. Another consequence of increasing head-groups is increasing distance between ends of alkyl chains in the series **im18**, **bim18**, **nim18** which likely diminishes the ability to form a well-ordered aliphatic sublattice which is apparent from the low intensity of the alkyl halo in the XRD profiles. Therefore, the observed small calorimetric effect for **nim18** is consistent with partial melting involving some part of the alkyl chains.

No peaks can be associated with the thermally driven SCO process in the DSC profiles of the compounds because of continuous processes giving undetectable variation of the heat flow.

Thin Films of mpy18. Compounds **im18** and **bim18** are thermochromic, changing color upon cooling from red-brown to red-violet and from violet to blue, respectively, due to SCO from HS to LS states. Compound **mpy18** exhibits especially pronounced thermochromic properties reversibly changing color upon cooling from red-wine to dark violet. This pronounced thermochromic property and perfect solubility in chloroform encouraged us to check a possibility of preparing thin films of **mpy18** and studying their magnetic properties which together with the thermochromism is related to the change of the electronic structure of Fe^{II} ions.[4] Deposited by a spin-coating technique (Figure S11 in the SI), the thin films of the compound retain the magnetic properties as follows from comparison of $\chi_M T$ vs T curves of the nonheated compound

dx.doi.org/10.1021/ic5010159 | Inorg. Chem. 2014, 53, 8442−8454

with that of the film mechanically peeled from the glass substrate (Figure 9). This proof of principle study demonstrates

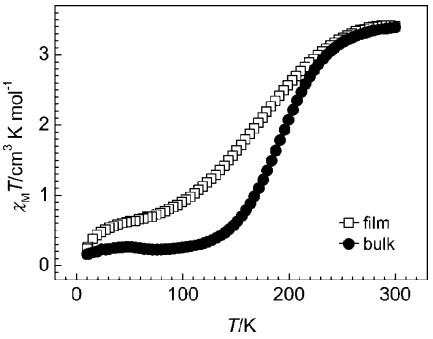

Figure 9. Thermal variation of the $\chi_M T$ vs T for a film and for a bulk of **mpy18**.

the ease of processability of the metallomesogens for thin films preparation without using the sophisticated Langmuir–Blodgett technique[21] and without substantial deterioration of SCO and therefore of thermochromic properties.

DISCUSSION

Complexes **mpy8**·0.5H_2O, **im4***·MeOH and **bim6** exhibit a star-like shape of complex molecules with radially protruding alkyl chains tethered to central coordination head-groups. The three compounds exhibit similar features of packing with discrepancies imposed by the length of the alkyl chains and the size of the head-groups. For **im4***·MeOH with the compact head-group a hexagonal packing of molecules is realized with columns formed by the head-groups surrounded by anions and alkyl chains. For **mpy8**·0.5H_2O and **bim6** larger head-groups with longer alkyl substituents form a lamellar structure where the cationic head-groups of the complex and anions form ionic monolayers while the alkyl substituents form aliphatic sublattice (Figure 10a). In the **A6** or **B12** with an elongated molecular shape a similar lamellar structure was observed with the only difference being that alkyl chains in complex molecules protrude in one direction; therefore, instead of an ionic monolayer, ionic bilayers are formed with a denser network of intermolecular bonds between complex head-groups and anions (Figure 10b). This has an important consequence on the magnetic and spectroscopic properties of the compounds. In crystalline Fe^{II} compounds with cooperative SCO, usually strong intermolecular contacts occur due to $\pi-\pi$ interactions, hydrogen bonds, and weak van der Waals contacts between complex molecules.[4] In the lattice, the intermolecular contacts transmit information between SCO centers about the spin state; therefore, any change of these contacts, e.g. due to loss of solvent or due to phase transitions leads to changes in the structure-dependent properties of the compound. This is the reason why, for example, polymorphs differing only in the type of the packing of molecules exhibit markedly different SCO behaviors.[22] In fact, in the case of a SCO compound a solid–solid or solid–liquid crystalline PT can be viewed as a reversible transformation between two polymorphs with concomitant steep change of the physical properties in the PT point.

It was suggested[11] that melting modifies mostly only structure-related parameters of the SCO transition, namely, the cooperativity. In our opinion, the reason for a moderate effect of the melting on the SCO properties in **imN** and **bimN** lies in the absence of strong interactions between SCO molecules in the solid state; therefore, melting and perturbation of the two-dimensional ionic monolayers does not have a pronounced effect on SCO properties. This behavior contrast with the reported earlier Fe^{II} metallomesogens **CN**, N = 12, 14, 16[10d] (Scheme 2) adapting bilayered packing and where a cooperative SCO was observed with the modification of cooperativity at the point of the PT crystal–liquid crystal.[10d]

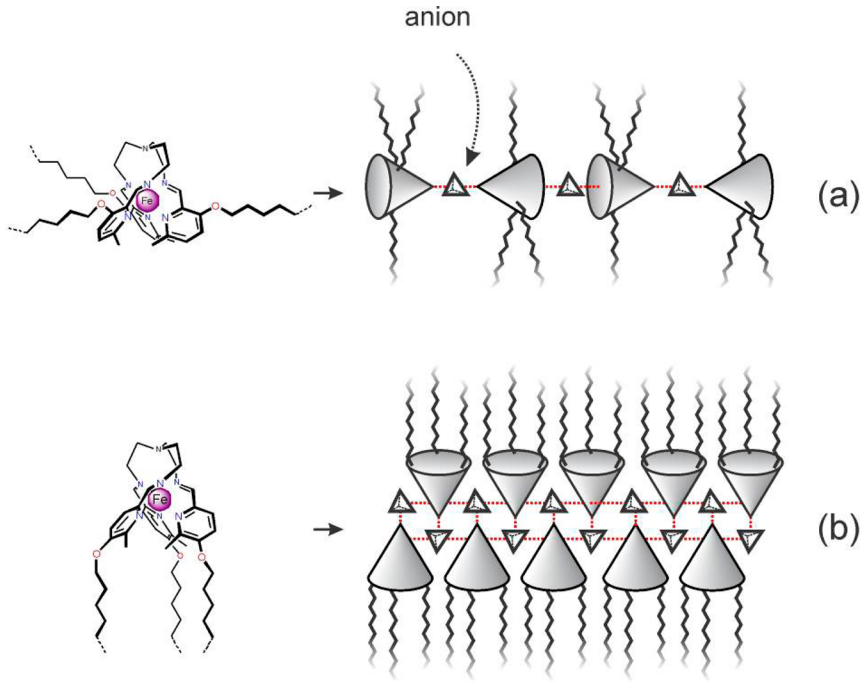

Figure 10. Schematic comparison of a monolayer in **mpy8** (a) and a bilayer in **A6** (b). Dashed lines represent intermolecular contacts.

dx.doi.org/10.1021/ic5010159 | Inorg. Chem. 2014, 53, 8442–8454

Taking into account results reported here and those accumulated from studies of Fe^{II} and Co^{II} SCO metallomesogens and valence tautomeric complexes,[17b,21,23] we conclude that the elongated molecular shape is preferable for more efficient interaction between PT and SCO. Also important are strong interactions between the neighboring head-groups; therefore, it is essential to utilize ligands forming hydrogen bonds or exhibiting $\pi-\pi$ stacking interactions which would "lock" variation of the spin state before melting. For example, derivatives of large planar heterocyclic molecules might be useful for this purpose. Finally, the complex molecule must possess an optimal number of alkyl substituents to form a well-organized aliphatic sublattice responsible for perturbation of the interactions upon melting. For this end branched alkyl chains or alkoxyphenyl substituents can be utilized, which also serve for tuning the melting point (see examples in ref 21). The synthesis, structure, and properties of new materials will be reported in due course.

In summary, here we have described three new families of mononuclear metallomesogens exhibiting SCO (**mpyN**, **imN**, and **bimN**). The short-chain compounds behave as normal crystalline compounds; however, lengthening the alkyl chains leads to the appearance of liquid crystalline properties and, more importantly, to influence of the PT crystal−liquid crystal on SCO properties of the compounds. Due to solubility in chloroform, these bifunctional materials can be obtained in the form of thin films retaining magnetic and thermochromic properties of the bulk material.

EXPERIMENTAL SECTION

Physical Measurements. Variable-temperature magnetic susceptibility data were recorded with a Quantum Design MPMS2 SQUID susceptometer equipped with a 7 T magnet, operating at 1 T and at temperatures 10−400 K. Experimental susceptibilities were corrected from diamagnetism of the constituent atoms by the use of Pascal's constants. TGA measurements were performed on a Mettler Toledo TGA/SDTA 851e, in the 150−400 K temperature range under a nitrogen atmosphere with a rate of 10 K min^{-1}. Analysis for C, H, and N were performed after combustion at 850 °C using IR detection and gravimetry by means of a PerkinElmer 2400 series II device. ^1H and ^{13}C NMR spectroscopic measurements were done on an Avance DRX Bruker 300 MHz spectrometer. IR spectra were recorded at 293 K by using a Nicolet 5700 FTIR spectrometer with the samples prepared as KBr discs. X-ray measurements where performed on a Seifert TT3300 diffractometer (monochromatic Cu Kα radiation). Mass spectroscopic studies were performed on a WATERS ZQ.

Single-Crystal X-ray Diffraction. Single-crystal X-ray data of **mpy8**·0.5H_2O, **im4**·MeOH, and **bim6** were collected on a Nonius Kappa-CCD single-crystal diffractometer using graphite monochromated Mo Kα radiation (λ = 0.71073 Å). A multiscan absorption correction was performed. The structures were solved by direct methods using SHELXS-97 and refined by full-matrix least-squares on F^2 using SHELXL-97.[25] Non-hydrogen atoms were refined anisotropically, and hydrogen atoms were placed in calculated positions refined using idealized geometries (riding model) and assigned fixed isotropic displacement parameters. CCDC files 975036−975041 contain the supplementary crystallographic data for this paper. These data can be obtained free of charge from The Cambridge Crystallographic Data Centre via www.ccdc.cam.ac.uk/data_request/cif.

MATERIALS

Synthesis of the Ligands. All chemicals were purchased from commercial sources and used without further purification. 2-(Diethoxymethyl)-1*H*-benzimidazole and 1*H*-naphtho[2,3-*d*]imidazole-2-carbaldehyde were synthesized according to the reported procedures.[24]

3-Hydroxy-6-methylpicolinaldehyde (Scheme 1a in the SI). To commercial 2-(hydroxymethyl)-6-methylpyridin-3-ol (10 g, 71.9 mmol) suspended in CH_2Cl_2 was added 66 g of active MnO_2. The slurry was stirred at RT for 24 h and then filtered twice through a pad of Celite. The yellow filtrate was evaporated to dryness. The obtained crystalline residue was analytically pure 3-hydroxy-6-methylpicolinaldehyde. Yield 7.3 g (75%). ^1H NMR (300 MHz, $CDCl_3$): δ (ppm) 10.64 (1H, s, OH), 10.02 (1H, s, CHO), 7.28 (2H, m, $PyH^{4,5}$), 2.56 (3H, s, CH_3); ^{13}C NMR (100 MHz, $CDCl_3$): δ (ppm) 198.7 (CHO), 156.9, 136.6, 130.4, 126.4, 23.5. FT-IR (KBr; cm^{-1}): 1651 ν(C═O). MS ESI (rel. int.): *m*/*z* 138.05 $[M + H]^+$ (100%). Elemental analysis calcd for $C_7H_7NO_2$: C, 61.31; H, 5.14; N, 10.21. Found C, 61.35; H, 5.13; N, 10.11.

Standard Procedure for 3-Alkoxy-6-methylpicolinaldehyde (Scheme S1a in the SI) and 1-Alkyl-1*H*-imidazole-2-carbaldehyde (Scheme S1b in the SI). 3-Hydroxy-6-methylpicolinaldehyde (1.00 g, 7.30 mmol) or commercial 1*H*-imidazole-2-carbaldehyde (0.70 g, 7.30 mmol), anhydrous potassium carbonate (1.00 g, 7.30 mmol), and *n*-alkyl bromide (7.30 mmol) were stirred vigorously in dry *N*,*N*-dimethylformamide (30 mL) at 100 °C for 3−4 h. After cooling, to the reaction mixture was added an excess of water. Then an oil or precipitate was formed depending on the length of the alkyl substituents; the oil was extracted by *n*-hexane while the precipitate was filtered off and recrystallized from ethanol and then dried *in vacuo*, providing an analytically pure product.

3-Octyloxy-6-methylpicolinaldehyde. From 1.41 g of *n*-octyl bromide. Yellow-brown oil, quantitative yield. Compound was used without purification. ^1H NMR (300 MHz, $CDCl_3$): δ (ppm) 10.43 (1H, s, CHO), 7.33 (2H, m, PyH), 4.08 (2H, t, *J* = 6.6 Hz, OCH_2), 2.59 (3H, s, CH_3), 1.86 (2H, quin, *J* = 6.6 Hz, OCH_2CH_2), 1.48 (2H, quin, *J* = 6.6 Hz, $OCH_2CH_2CH_2$), 1.32 (8H, m, CH_2), 0.90 (3H, t, *J* = 6.6 Hz, CH_3). ^{13}C NMR (100 MHz, $CDCl_3$): δ (ppm) 190.1, 156.9, 151.1, 140.8, 129.3, 122.5, 69.5, 32.2, 29.7, 29.6, 29.4, 26.3, 23.8, 23.1, 14.5. MS ESI (rel. int.): *m*/*z* 250.18 $[M + H]^+$ (100%).

3-Octadecyloxy-6-methylpicolinaldehyde. From 2.43 g of *n*-octadecyl bromide. White solid, yield 2.81 g (99%). ^1H NMR (300 MHz, $CDCl_3$): δ (ppm) 10.41 (1H, s, CHO), 7.31 (2H, m, PyH), 4.07 (2H, t, *J* = 6.6 Hz, OCH_2), 2.57 (3H, s, CH_3), 1.86 (2H, quin, *J* = 6.6 Hz, OCH_2CH_2), 1.48 (2H, quin, *J* = 6.6 Hz, $OCH_2CH_2CH_2$), 1.26 (28H, m, CH_2), 0.88 (3H, t, *J* = 6.6 Hz, CH_3). ^{13}C NMR (100 MHz, $CDCl_3$): δ (ppm) 189.9, 187.5, 156.9, 147.8, 128.7, 121.9, 69.1, 31.9, 29.3 m, 25.9, 23.5, 22.7, 14.1. FT-IR (KBr; cm^{-1}): 1651 ν(C═O). MS ESI (rel. int.): *m*/*z* 390.34 $[M + H]^+$ (100%). Elemental analysis calcd (%) for $C_{25}H_{43}NO_2$: C, 77.07; H, 11.12; N, 3.60; found C, 77.20; H, 10.61; N 3.53.

1-Butyl-1*H*-imidazole-2-carbaldehyde. From 1.00 g of *n*-buthyl bromide. Yellow oil, yield 0.99 g (90%). Compound was used without purification. ^1H NMR (300 MHz, $CDCl_3$): δ (ppm) 9.81 (1H, s, CHO), 7.28 (1H, d, *J* = 0.8 Hz, imH^5), 7.16 (1H, d, *J* = 0.8 Hz, imH^4), 4.40 (2H, t, *J* = 7.3 Hz, NCH_2), 1.76 (2H, m, NCH_2CH_2), 1.34 (2H, m, $NCH_2CH_2CH_2$), 0.95 (3H, t, *J* = 7.3 Hz, CH_3). ^{13}C NMR (100 MHz, $CDCl_3$): δ (ppm) 182.4 (CHO), 143.7, 131.9, 126.6, 47.9, 33.4, 20.0, 13.9. MS ESI (rel. int.): *m*/*z* 153.10 $[M + H]^+$ (100%).

1-Hexadecyl-1*H*-imidazole-2-carbaldehyde. From 2.23 g of *n*-hexadecyl bromide. Yellow solid, yield 1.97 g (84%). ^1H NMR (300 MHz, $CDCl_3$): δ (ppm) 9.79 (1H, s, CHO), 7.24

dx.doi.org/10.1021/ic5010159 | Inorg. Chem. 2014, 53, 8442−8454

(1H, s, imH), 7.12 (1H, s, imH), 4.35 (2H, t, J = 7.3 Hz, NCH_2), 1.74 (2H, m, NCH_2CH_2), 1.28−1.12 (26H, m, CH_2), 0.85 (3H, t, J = 7.3 Hz, CH_3). ^{13}C NMR (100 MHz, $CDCl_3$): δ (ppm) 182.3 (CHO), 143.6, 131.7, 126.6, 48.3, 32.3−29.5, 26.8, 23.1, 14.5. MS ESI (rel. int.): m/z 321.29 $[M + H]^+$ (100%). Elemental analysis calcd (%) for $C_{20}H_{36}N_2O$: C, 74.95; H, 11.32; N, 8.74; found 74.67; 10.99; 8.91.

1-Octadecyl-1*H*-imidazole-2-carbaldehyde. From 2.43 g of *n*-octadecyl bromide. Yellow solid, yield 2.54 g (85%). ^{1}H NMR (300 MHz, $CDCl_3$): δ (ppm) 9.76 (1H, s, CHO), 7.22 (1H, s, imH), 7.09 (1H, s, imH), 4.32 (2H, t, J = 7.3 Hz, NCH_2), 1.70 (2H, m, NCH_2CH_2), 1.28−1.12 (30H, m, CH_2), 0.81 (3H, t, J = 7.3 Hz, CH_3). ^{13}C NMR (100 MHz, $CDCl_3$): δ (ppm) 182.3 (CHO), 143.6, 131.7, 126.6, 48.3, 32.3−29.5, 26.8, 23.1, 14.6. MS ESI (rel. int.): m/z 349.32 $[M + H]^+$ (100%). Elemental analysis calcd (%) for $C_{22}H_{40}N_2O$: C, 75.81; H, 11.57; N, 8.04; found C, 75.41; H, 10.95; N, 7.94.

1-Eicosyl-1*H*-imidazole-2-carbaldehyde. From 2.64 g of *n*-eicosyl bromide. Yellow solid, yield 2.42 g (88%). ^{1}H NMR (300 MHz, $CDCl_3$): δ (ppm) 9.73 (1H, s, CHO), 7.20 (1H, s, imH), 7.07 (1H, s, imH), 4.31 (2H, t, J = 7.3 Hz, NCH_2), 1.70 (2H, m, NCH_2CH_2), 1.30−1.12 (34H, m, CH_2), 0.80 (3H, t, J = 7.3 Hz, CH_3). ^{13}C NMR (100 MHz, $CDCl_3$): δ (ppm) 182.4 (CHO), 143.7, 131.9, 126.6, 48.2, 32.3−29.5, 26.8, 23.1, 14.5. MS ESI (rel. int.): m/z 377.35 $[M + H]^+$ (100%). Elemental analysis calcd (%) for $C_{24}H_{44}N_2O$: C, 76.54; H, 11.78; N, 7.44; found C, 76.75, H, 11.19, N, 7.06.

1-Docosyl-1*H*-imidazole-2-carbaldehyde. From 2.84 g of *n*-docosyl bromide. Yellow solid, yield 2.21 g (75%). ^{1}H NMR (300 MHz, $CDCl_3$): δ (ppm) 9.81 (1H, s, CHO), 7.28 (1H, s, imH), 7.15 (1H, s, imH), 4.38 (2H, t, J = 7.3 Hz, NCH_2), 1.77 (2H, m, NCH_2CH_2), 1.30−1.12 (38H, m, CH_2), 0.88 (3H, t, J = 7.3 Hz, CH_3). ^{13}C NMR (100 MHz, $CDCl_3$): δ (ppm) 182.4 (CHO), 143.7, 131.9, 126.6, 48.3, 32.3−29.5, 26.8, 23.1, 14.5. MS ESI (rel. int.): m/z 405.38 $[M + H]^+$ (100%). Elemental analysis calcd (%) for $C_{26}H_{44}N_2O$: C, 77.94; H, 11.07; N, 6.99; found C, 77.73; H, 11.16; N, 6.56.

Standard Procedure for 1-Alkyl-1*H*-benzoimidazole-2-carbaldehyde and 1-Alkyl-1*H*-naphtho[2,3-*d*]-imidazole-2-carbaldehyde (Scheme S1b,c in the SI). 1-Alkyl-2-(diethoxymethyl)-1*H*-benzimidazole and 2-(diethoxymethyl)-1-alkyl-1*H*-naphtho[2,3-*d*]imidazole prepared from 2-(diethoxymethyl)-1*H*-benzimidazole or 2-(diethoxymethyl)-1*H*-naphtho[2,3-*d*]imidazole, respectively, by a procedure similar to that of 1-alkyl-1*H*-imidazole-2-carbaldehyde described above, were hydrolyzed by refluxing 24 h in a mixture of 4 N HCl_{aq} and THF (1:2). After cooling, the reaction mixture was neutralized with sodium carbonate and extracted with EtOAc (3 × 50 mL). The extract was washed with water (5 × 30 mL) and brine, dried by $MgSO_4$, filtered, and evaporated. The residue was recrystallized twice from EtOH and dried *in vacuo*.

1-Hexyl-1*H*-benzimidazole-2-carbaldehyde. Yellow-brown oil, which partially crystallizes upon standing; yield 45% [relatively 2-(diethoxymethyl)-1*H*-benzimidazole]. ^{1}H NMR (300 MHz, $CDCl_3$): δ (ppm) 10.11 (1H, s, CHO), 7.93 (1H, dt, J = 1.0, 8.1 Hz, ArH), 7.43 (3H, m, ArH), 4.59 (2H, t, J = 7.4 Hz, NCH_2), 1.82 (2H, quin, J = 7.4 Hz, NCH_2CH_2), 1.31 (6H, m, CH_2), 0.87 (3H, t, J = 7.4 Hz, CH_3). ^{13}C NMR (100 MHz, $CDCl_3$): δ (ppm) 185.3 (CHO), 146.4, 143.2, 136.8, 127.1, 124.4, 122.8, 111.4, 45.3, 31.8, 30.7, 26.8, 22.9, 14.4. MS ESI (rel. int.): m/z 231.15 $[M + H]^+$ (100%). Elemental analysis calcd (%) for $C_{14}H_{18}N_2O$: C, 73.01; H, 7.88; N, 12.16; found C, 72.57; H, 7.35; N, 12.10.

1-Tetradecyl-1*H*-benzimidazole-2-carbaldehyde. Off-white solid, yield 50% [relatively 2-(diethoxymethyl)-1*H*-benzimidazole]. ^{1}H NMR (300 MHz, $CDCl_3$): δ (ppm) 10.10 (1H, s, CHO), 7.95 (1H, dt, J = 1.0, 8.1 Hz, ArH), 7.44 (3H, m, ArH), 4.55 (2H, t, J = 7.4 Hz, NCH_2), 1.80 (2H, quin, J = 7.4 Hz, NCH_2CH_2), 1.31−1.22 (22H, m, CH_2), 0.87 (3H, t, J = 7.4 Hz, CH_3). ^{13}C NMR (100 MHz, $CDCl_3$): δ (ppm) 185.3 (CHO), 146.4, 143.2, 136.8, 127.1, 124.4, 122.8, 111.4, 45.3, 32.3−29.3, 27.1, 23.1, 18.8, 14.5. MS ESI (rel. int.): m/z 343.27 $[M + H]^+$ (100%). Elemental analysis calcd (%) for $C_{22}H_{34}N_2O$: C, 77.14; H, 10.01; N, 8.18; found C, 76.94; H, 9.96; N, 8.60.

1-Hexadecyl-1*H*-benzimidazole-2-carbaldehyde. Off-white solid, yield 54% [relatively 2-(diethoxymethyl)-1*H*-benzimidazole]. ^{1}H NMR (300 MHz, $CDCl_3$): δ (ppm) 10.12 (1H, s, CHO), 7.95 (1H, dt, J = 1.0, 8.1 Hz, ArH), 7.44 (3H, m, ArH), 4.56 (2H, t, J = 7.4 Hz, NCH_2), 1.84 (2H, quin, J = 7.4 Hz, NCH_2CH_2), 1.31−1.22 (26H, m, CH_2), 0.87 (3H, t, J = 7.4 Hz, CH_3). ^{13}C NMR (100 MHz, $CDCl_3$): δ (ppm) 185.3 (CHO), 146.4, 143.2, 136.8, 127.1, 124.4, 122.8, 111.4, 45.3, 32.3−29.3, 27.1, 23.1, 18.8, 14.5. MS ESI (rel. int.): m/z 371.32 $[M + H]^+$ (100%). Elemental analysis calcd (%) for $C_{24}H_{38}N_2O$: C, 77.79; H, 10.34; N, 7.56; found C, 77.44; H, 10.00; N, 7.43.

1-Octadecyl-1*H*-benzimidazole-2-carbaldehyde. Off-white solid, yield 54% [relatively 2-(diethoxymethyl)-1*H*-benzimidazole]. ^{1}H NMR (300 MHz, $CDCl_3$): δ (ppm) 10.13 (1H, s, CHO), 7.95 (1H, dt, ArH), 7.45 (3H, m, ArH), 4.61 (2H, t, J = 7.4 Hz, NCH_2), 1.85 (2H, m, NCH_2CH_2), 1.33−1.23 (30H, m, CH_2), 0.89 (3H, t, J = 7.4 Hz, CH_3). ^{13}C NMR (100 MHz, $CDCl_3$): δ (ppm) 185.3 (CHO), 146.4, 143.2, 136.8, 127.1, 124.4, 122.8, 111.4, 45.3, 32.3−29.3, 27.2, 23.1, 18.8, 14.5. MS ESI (rel. int.): m/z 399.33 $[M + H]^+$ (100%). Elemental analysis calcd (%) for $C_{26}H_{42}N_2O$: C, 78.34; H, 10.62; N, 7.03; found 78.55; 10.39; 6.63.

1-Eicosyl-1*H*-benzimidazole-2-carbaldehyde. Off-white solid, yield 57% [relatively 2-(diethoxymethyl)-1*H*-benzimidazole]. ^{1}H NMR (300 MHz, $CDCl_3$): δ (ppm) 10.13 (1H, s, CHO), 7.95 (1H, dt, ArH), 7.45 (3H, m, ArH), 4.61 (2H, t, J = 7.4 Hz, NCH_2), 1.85 (2H, m, NCH_2CH_2), 1.33−1.23 (34H, m, CH_2), 0.89 (3H, t, J = 7.4 Hz, CH_3). ^{13}C NMR (100 MHz, $CDCl_3$): δ (ppm) 185.3 (CHO), 146.4, 143.2, 136.8, 127.1, 124.4, 122.8, 111.4, 45.3, 32.3−29.6, 27.2, 23.1, 18.8, 14.5. MS ESI (rel. int.): m/z 427.35 $[M + H]^+$ (100%). Elemental analysis calcd (%) for $C_{28}H_{46}N_2O$: C, 78.82; H, 10.87; N, 6.57; found C, 78.48; H, 10.39; N, 6.24.

1-Octadecyl-1*H*-naphtho[2,3-*d*]imidazole-2-carbaldehyde. Yellow solid, yield 60% [relatively 2-(diethoxymethyl)-1*H*-naphtho[2,3-*d*]imidazole]. ^{1}H NMR (300 MHz, $CDCl_3$): δ (ppm) 10.22 (1H, s, CHO), 8.49 (1H, s, ArH), 8.05 (1H, d, J = 7.6 Hz, ArH), 7.98 (1H, d, J = 7.6 Hz, ArH), 7.90 (1H, s, ArH), 7.48 (2H, m, ArH), 4.70 (2H, t, J = 7.4 Hz, NCH_2), 1.91 (2H, quin, J = 7.4 Hz, NCH_2CH_2), 1.40−1.23 (30H, m, CH_2), 0.90 (3H, t, J = 7.4 Hz, CH_3). ^{13}C NMR (100 MHz, $CDCl_3$): δ (ppm) 185.8 (CHO), 149.4, 142.8, 136.8, 133.0, 131.4, 129.3, 128.0, 126.2, 124.5, 120.6, 107.2, 45.3, 32.3, 30.1−29.7 (m), 27.2, 23.1, 14.5. MS ESI (rel. int.): m/z 449.35 $[M + H]^+$ (100%). Elemental analysis calcd (%) for $C_{30}H_{44}N_2O$: C, 80.31; H, 9.88; N, 6.24; found C, 80.04; H, 9.99; N, 5.96.

dx.doi.org/10.1021/ic5010159 | *Inorg. Chem.* 2014, 53, 8442−8454

SYNTHESIS OF COMPLEXES

General Procedure (Scheme S2 in the SI). A batch of an alkylated aldehyde (1 mmol) and tris(2-aminoethyl)amine (tren) (0.05 g, 0.34 mmol) were dissolved in absolute ethanol (10 mL) upon heating; the calculated amount of iron(II) tetrafluoroborate hexahydrate (0.12 g, 0.34 mmol) or iron(II) perchlorate hexahydrate (0.13 g, 0.34 mmol) was added which was immediately accompanied by intensive coloration. While boiling, the mixture was stirred for 15 min and after cooling to ambient temperature was transferred into a refrigerator and left at 4 °C overnight. The formed crystalline precipitate was filtered off, washed with ethanol, and dried *in vacuo*.

***mpy8*·0.5H_2O.** From excess of crude 3-octyloxy-6-methylpicolinaldehyde. Deep red block crystals form after a week in refrigerator. Yield 0.21 g (57%). FT-IR (KBr; cm^{-1}): 2926, 2854 ν(C−H), 1639 ν(C═N), 1060 ν(B−F). MS ESI (rel. int.): m/z 982.68 $[M + BF_4]^+$ (100%), 448.11 $[M]^{+2}$ (50%). Elemental analysis calcd (%) for $C_{51}H_{82}B_2F_8FeN_7O_{3.5}$: C, 56.79; H, 7.66; N, 9.09; found C, 56.56; H, 7.26; N, 9.20.

***mpy18*.** From 3-octadecyloxy-6-methylpicolinaldehyde (0.39 g). Wine-red powder. Yield 0.40 g (79%). FT-IR (KBr; cm^{-1}): 2919, 2849 ν(C−H), 1639 ν(C═N), 1058 ν(B−F). MS ESI (rel. int.): m/z 1403.04 $[M + BF_4]^+$ (100%), 658.06 $[M]^{+2}$ (23%). Elemental analysis calcd (%) for $C_{81}H_{141}B_2F_8FeN_7O_3$: C, 65.27; H, 9.54; N, 6.58; found C, 65.17; H, 8.96; N, 6.64.

***im4*·*MeOH*.** From excess of crude 1-butyl-1*H*-imidazole-2-carbaldehyde. Red-brown crystals. Yield 0.23 g (85%) FT-IR (KBr; cm^{-1}): 2964, 2940, 2869 ν(C−H), 1620 ν(C═N), 1055 ν(B−F). MS ESI (rel. int.): m/z 691.48 $[M + BF_4]^+$ (100%), 302.39 $[M]^{+2}$ (65%). Elemental analysis calcd (%) for $C_{31}H_{52}B_2F_8FeN_{10}O$: C, 45.95; H, 6.47; N, 17.29; found C, 46.26; H, 6.63; N, 17.89.

***im4**·*MeOH*.** From excess of crude 1-butyl-1*H*-imidazole-2-carbaldehyde. Red-brown crystals. Yield 0.26 g (90%). FT-IR (KBr; cm^{-1}): 2920, 2850 ν(C−H), 1683, 1621 ν(C═N), 1191 ν(Cl−O). MS ESI (rel. int.): m/z 703.43 $[M + ClO_4]^+$ (100%), 302.38 $[M]^{+2}$ (34%). Elemental analysis calcd (%) for $C_{31}H_{52}Cl_2FeN_{10}O_9$: C, 44.56; H, 6.27; N, 16.76; found C, 45.10; H, 6.57; N, 17.43.

***im16*.** From 1-hexadecyl-1*H*-imidazole-2-carbaldehyde (0.32 g). Red-brown powder. Yield 0.37 g (78%). FT-IR (KBr; cm^{-1}): 2920, 2850 ν(C−H), 1681, 1624 ν(C═N), 1061 ν(B−F). MS ESI (rel. int.): m/z 1195.91 $[M + BF_4]^+$ (100%), 554.48 $[M]^{+2}$ (14%). Elemental analysis calcd (%) for $C_{66}H_{120}B_2F_8FeN_{10}$: C, 61.78; H, 9.43; N, 10.92; found C, 61.70; H, 8.97; N, 10.91.

***im18*.** From 1-octadecyl-1*H*-imidazole-2-carbaldehyde (0.35 g). Red-brown powder. Yield 0.43 g (93%). FT-IR (KBr; cm^{-1}): 2919, 2851 ν(C−H), 1680, 1623 ν(C═N), 1061 ν(B−F). MS ESI (rel. int.): m/z 1279.96 $[M + BF_4]^+$ (100%), 596.73 $[M]^{+2}$ (22%). Elemental analysis calcd (%) for $C_{72}H_{132}B_2F_8FeN_{10}$: C, 63.24; H, 9.73; N, 10.24; found C, 63.34; N, 9.23; N, 10.53.

***im20*.** From 1-eicosyl-1*H*-imidazole-2-carbaldehyde (0.38 g). Red-brown powder. Yield 0.47 g (95%). FT-IR (KBr; cm^{-1}): 2919, 2851 ν(C−H), 1680, 1623 ν(C═N), 1061 ν(B−F). MS ESI (rel. int.): m/z 1364.10 $[M + BF_4]^+$ (100%), 638.57 $[M]^{+2}$ (13%). Elemental analysis calcd (%) for $C_{78}H_{144}B_2F_8FeN_{10}$: C, 64.54; H, 10.00; N, 9.65; found C, 64.64; H, 9.60; N, 9.11.

***im22*.** From 1-docosyl-1*H*-imidazole-2-carbaldehyde (0.41 g). Red-brown powder. Yield 0.47 g (91%). FT-IR (KBr; cm^{-1}): 2919, 2851 ν(C−H), 1680, 1623 ν(C═N), 1061 ν(B−F). MS ESI (rel. int.): m/z 1448.19 $[M + BF_4]^+$ (100%), 680.55 $[M]^{+2}$ (14%). Elemental analysis calcd (%) for $C_{84}H_{156}B_2F_8FeN_{10}$: C, 65.70; H, 10.24; N, 9.12; found C, 65.44; H, 10.93; N, 8.80.

***bim6*.** From 1-hexyl-1*H*-benzimidazole-2-carbaldehyde (0.23 g). Violet plate crystals. Yield 0.31 g (63%). FT-IR (KBr; cm^{-1}): 2953 sh, 2930, 2856 ν(C−H), 1637, 1618 ν(C═N), 1192 ν(Cl−O). MS ESI (rel. int.): m/z 937.42 $[M + ClO_4]^+$ (100%), 419.29 $[M]^{+2}$ (17%). Elemental analysis calcd (%) for $C_{48}H_{66}Cl_2FeN_{10}O_8$: C, 55.55; H, 6.41; N, 13.50; found C, 55.40; H, 6.16; N, 13.65.

***bim14*.** From 1-tetradecyl-1*H*-benzimidazole-2-carbaldehyde (0.34 g). Violet powder. Yield 0.42 g (90%). FT-IR (KBr; cm^{-1}): 2917, 2854 ν(C−H), 1625 ν(C═N), 1192 ν(Cl−O). MS ESI (rel. int.): m/z 1273.82 $[M + ClO_4]^+$ (100%), 587.45 $[M]^{+2}$ (10%). Elemental analysis calcd (%) for $C_{72}H_{114}Cl_2FeN_{10}O_8$: C, 62.92; H, 8.36; N, 10.19; found C, 62.72; H, 8.88; N, 9.89.

***bim16*.** From 1-hexadecyl-1*H*-benzimidazole-2-carbaldehyde (0.37 g). Violet powder. Yield 0.42 g (85%). FT-IR (KBr; cm^{-1}): 2919, 2854 ν(C−H), 1625 ν(C═N), 1191 ν(Cl−O). MS ESI (rel. int.): m/z 1357.93 $[M + ClO_4]^+$ (100%), 629.45 $[M]^{+2}$ (9%). Elemental analysis calcd (%) for $C_{78}H_{126}Cl_2FeN_{10}O_8$: C, 64.23; H, 8.71; N, 9.60; found C, 64.31; H, 9.01; N, 9.63.

***bim18*.** From 1-octadecyl-1*H*-benzimidazole-2-carbaldehyde (0.39 g). Violet powder. Yield 0.50 g (96%). FT-IR (KBr; cm^{-1}): 2920, 2849 ν(C−H), 1625 ν(C═N), 1090 ν(Cl−O). MS ESI (rel. int.): m/z 1441.96 $[M + ClO_4]^+$ (100%), 671.55 $[M]^{+2}$ (7%). Elemental analysis calcd (%) for $C_{84}H_{138}Cl_2FeN_{10}O_8$: C, 65.39; H, 9.02; N, 9.08; found C, 65.12; H, 8.57; N, 9.56.

***bim20*.** From 1-eicosyl-1*H*-benzimidazole-2-carbaldehyde (0.43 g). Violet powder. Yield 0.54 g (97%). FT-IR (KBr; cm^{-1}): 2920, 2851 ν(C−H), 1622 ν(C═N), 1091 ν(Cl−O). MS ESI (rel. int.): m/z 1526.11 $[M + ClO_4]^+$ (100%). Elemental analysis calcd (%) for $C_{90}H_{150}Cl_2FeN_{10}O_8$: C, 67.49; H, 9.44; N, 8.75; found C, 67.79; H, 10.05; N, 8.25.

***nim18*.** From 1-octadecyl-1*H*-naphtho[2,3-*d*]imidazole-2-carbaldehyde (0.45 g). Green, sticky powder. Yield 0.57 g (99%). FT-IR (KBr; cm^{-1}): 2922, 2850 ν(C−H), 1620 ν(C═N), 1094 ν(Cl−O). MS ESI (rel. int.): m/z 746.64 $[M]^{+2}$ (7%). Elemental analysis calcd (%) for $C_{96}H_{150}Cl_2FeN_{10}O_8$: C, 67.86; H, 8.90; N, 8.24; C, 67.03, H, 8.18, N, 8.20.

ASSOCIATED CONTENT

Supporting Information

Schematic synthesis of the alkylated heterocyclic aldehydes and of the complexes. Mössbauer spectroscopic data for **mpy8**, **mpy18**, **im4**·MeOH, **bim6**, **im18**, **bim18**, and **im4*** at two representative temperatures (Figures S1 and S2 and Table S1). Thermal variation of the $\chi_M T$ product for **im16**, **im20**, **im22**, **bim14**, **bim16**, and **bim20** (Figure S3). Thermogravimetric data for **mpy8**·0.5H_2O, **mpy18**, **im4**·MeOH, **im18**, **bim6**, **bim18**, and **nim18** (Figure S4). Overlay of LS and HS complex molecules of **mpy8**·0.5H_2O at 120 and 200 K (Figure S5). Comparison of experimental diffraction pattern of **im4**·MeOH with the calculated diffraction pattern from X-ray single-crystal data of isomorphous **im4***·MeOH (Figure S6). The cavities within a cut of the structure of **im4***·MeOH along *c* (Figure S7). Diffractograms of **im16**, **im20**, **im22**, **bim14**, **bim16**, **bim20** at 300, 400, and back at 300 K (Figure S8). Theoretically estimated length of stretched **im18** (Figure S9).

dx.doi.org/10.1021/ic5010159 | *Inorg. Chem.* 2014, 53, 8442−8454

Interlayer distance d as a function of N, for the series **imN** and **bimN** at different temperatures (Figure S10). Photograph of films of **mpy18** of two thicknesses on glass substrate (Figure S11). Crystallographic data in CIF format of **bim6** (120 and 298 K), **im4*** (120 and 250 K), and **mpy8** (120 and 200 K). This material is available free of charge via the Internet at http://pubs.acs.org.

AUTHOR INFORMATION

Corresponding Authors

*E-mail: mcs@univ.kiev.ua; mlseredyuk@gmail.com.
*E-mail: jose.a.real@uv.es.

Present Address

[&]Taras Shevchenko National University, Department of Physical Chemistry, Volodymyrska Str. 64, Kyiv 01601, Ukraine.

Notes

The authors declare no competing financial interest.

ACKNOWLEDGMENTS

This work was supported by the Spanish Ministerio de Economía y Competitividad (MINECO) and FEDER funds (CTQ2013-46275-P), the Generalitat Valenciana through PROMETEO/2012/049 and ACOMP2012/233. Y.G. is grateful for grants RFBR 14-03-00136a and RSF-14-13-00758. M.S. thanks the EU for a Marie Curie fellowship (IIF-253254).

REFERENCES

(1) (a) Cambi, L.; Szegö, L. *Ber. Deutsch. Chem. Ges.* **1931**, *64*, 2591−2598. (b) Cambi, L.; Szegö, L. *Ber. Deutsch. Chem. Ges.* **1933**, *66*, 656−661. (c) Cambi, L.; Malatesta, L. *Ber. Deutsch. Chem. Ges.* **1937**, *70*, 2067−2078.

(2) (a) Bousseksou, A.; Vieu, C.; Létard, J.-F.; Demont, P.; Tuchagues, J.-P.; Malaquin, L.; Menegotto, G.; Salmon, L. F1430552, 2004. (b) Kahn, O.; Martinez, J. *Science* **1998**, *279*, 44−48.

(3) (a) Meded, V.; Bagrets, A.; Fink, K.; Chandrasekar, R.; Ruben, M.; Evers, F.; Bernand-Mantel, A.; Seldenthuis, J. S.; Beukman, A.; van der Zant, H. S. J. *Phys. Rev. B* **2011**, *83*, 245415. (b) Prins, F.; Monrabal-Capilla, M.; Osorio, E. A.; Coronado, E.; van der Zant, H. S. J. *Adv. Mater.* **2011**, *23*, 1545−1549. (c) Miyamachi, T.; Gruber, M.; Davesne, V.; Bowen, M.; Boukari, S.; Joly, L.; Scheurer, F.; Rogez, G.; Yamada, T. K.; Ohresser, P.; Beaurepaire, E.; Wulfhekel, W. *Nat. Commun.* **2012**, *3*, 938.

(4) Gütlich, P.; Goodwin, H. A. *Top. Curr. Chem.* **2004**, *233*, 1−47.

(5) Gütlich, P.; Hauser, A.; Spiering, H. *Angew. Chem., Int. Ed.* **1994**, *33*, 2024−2054.

(6) Seredyuk, M.; Gaspar, A. B.; Kusz, J.; Bednarek, G.; Gütlich, P. *J. Appl. Crystallogr.* **2007**, *40*, 1135−1145.

(7) (a) Müller, E. W.; Ensling, J.; Spiering, H.; Gütlich, P. *Inorg. Chem.* **1983**, *22*, 2074−2078. (b) Conti, A. J.; Kaji, K.; Nagano, Y.; Sena, K. M.; Yumoto, Y.; Chadha, R. K.; Rheingold, A. L.; Sorai, M.; Hendrickson, D. N. *Inorg. Chem.* **1993**, *32*, 2681−2693. (c) Létard, J. F.; Guionneau, P.; Codjovi, E.; Lavastre, O.; Bravic, G.; Chasseau, D.; Kahn, O. *J. Am. Chem. Soc.* **1997**, *119*, 10861−10862. (d) Chernyshov, D.; Hostettler, M.; Törnroos, K. W.; Bürgi, H. B. *Angew. Chem., Int. Ed.* **2003**, *42*, 3825−3830. (e) Hostettler, M.; Törnroos, K. W.; Chernyshov, D.; Vangdal, B.; Bürgi, H. B. *Angew. Chem., Int. Ed.* **2004**, *43*, 4589−4594. (f) Hayami, S.; Shigeyoshi, Y.; Akita, M.; Inoue, K.; Kato, K.; Osaka, K.; Takata, M.; Kawajiri, R.; Mitani, T.; Maeda, Y. *Angew. Chem., Int. Ed.* **2005**, *44*, 4899−4903. (g) Brefuel, N.; Imatomi, S.; Torigoe, H.; Hagiwara, H.; Shova, S.; Meunier, J. F.; Bonhommeau, S. B.; Tuchagues, J. P.; Matsumoto, N. *Inorg. Chem.* **2006**, *45*, 8126−8135. (h) Krivokapic, I.; Enachescu, C.; Bronisz, R.; Hauser, A. *Chem. Phys. Lett.* **2008**, *455*, 192−196. (i) Brefuel, N.; Watanabe, H.; Toupet, L.; Come, J.; Matsumoto, N.; Collet, E.; Tanaka, K.; Tuchagues, J.-P. *Angew. Chem., Int. Ed.* **2009**, *48*, 1−5. (j) Bhar, K.; Khan, S.; Costa, J. S.; Ribas, J.; Roubeau, O.; Mitra, P.; Ghosh, B. K. *Angew. Chem., Int. Ed.* **2012**, *51*, 2142−2145. (k) Seredyuk, M.; Muñoz, M. C.; Castro, M.; Romero-Morcillo, T.; Gaspar, A. B.; Real, J. A. *Chem.—Eur. J.* **2013**, *19*, 6591−6596.

(8) (a) Ozarowski, A.; McGarvey, B. R.; Sarkar, A. B.; Drake, J. E. *Inorg. Chem.* **1988**, *27*, 628−635. (b) Matouzenko, G. S.; Bousseksou, A.; Lecocq, S.; van Koningsbruggen, P. J.; Perrin, M.; Kahn, O.; Collet, A. *Inorg. Chem.* **1997**, *36*, 5869−5879. (c) Guionneau, P.; Létard, J. F.; Yufit, D. S.; Chasseau, D.; Bravic, G.; Goeta, A. E.; Howard, J. A. K.; Kahn, O. *J. Mater. Chem.* **1999**, *9*, 985−994. (d) Marchivie, M.; Guionneau, P.; Létard, J. F.; Chasseau, D. *Acta Crystallogr., Sect. B* **2003**, *59*, 479−486. (e) Galet, A.; Gaspar, A. B.; Muñoz, M. C.; Levchenko, G.; Real, J. A. *Inorg. Chem.* **2006**, *45*, 9670−9679.

(9) (a) Serrano, J. L. *Metallomesogens*; VCH: Weinheim, 1996. (b) Date, R. W.; Iglesias, E. F.; Rowe, K. E.; Elliott, J. M.; Bruce, D. W. *Dalton Trans.* **2003**, 1914−1931.

(10) (a) Seredyuk, M.; Gaspar, A. B.; Ksenofontov, V.; Reiman, S.; Galyametdinov, Y.; Haase, W.; Rentschler, E.; Gütlich, P. *Hyperfine Interact.* **2005**, *166*, 385−390. (b) Seredyuk, M.; Gaspar, A. B.; Ksenofontov, V.; Reiman, S.; Galyametdinov, Y.; Haase, W.; Rentschler, E.; Gütlich, P. *Chem. Mater.* **2006**, *18*, 2513−2519. (c) Seredyuk, M.; Gaspar, A. B.; Ksenofontov, V.; Galyametdinov, Y.; Kusz, J.; Gütlich, P. *J. Am. Chem. Soc.* **2008**, *130*, 1431−1439. (d) Seredyuk, M.; Gaspar, A. B.; Ksenofontov, V.; Galyametdinov, Y.; Kusz, J.; Gütlich, P. *Adv. Funct. Mater.* **2008**, *18*, 2089−2101. (e) Seredyuk, M.; Gaspar, A. B.; Ksenofontov, V.; Galyametdinov, Y.; Verdaguer, M.; Villain, F.; Gütlich, P. *Inorg. Chem.* **2008**, *47*, 10232−10245. (f) Seredyuk, M.; Gaspar, A. B.; Ksenofontov, V.; Galyametdinov, Y.; Verdaguer, M.; Villain, F.; Gütlich, P. *Inorg. Chem.* **2010**, *49*, 10022−10031. (g) Seredyuk, M. *Inorg. Chim. Acta* **2012**, *380*, 65−71.

(11) Gaspar, A. B.; Seredyuk, M.; Gütlich, P. *Coord. Chem. Rev.* **2009**, *253*, 2399−2413.

(12) (a) Decurtins, S.; Gütlich, P.; Köhler, C. P.; Spiering, H.; Hauser, A. *Chem. Phys. Lett.* **1984**, *105*, 1−4. (b) Létard, J. F. *J. Mater. Chem.* **2006**, *16*, 2550−2559.

(13) Seredyuk, M. Ph.D. Thesis; University of Mainz, 2008.

(14) Kirchner, R. M.; Mealli, C.; Bailey, M.; Howe, N.; Torre, L. P.; Wilson, L. J.; Andrews, L. C.; Rose, N. J.; Lingafelter, E. C. *Coord. Chem. Rev.* **1987**, *77*, 89−163.

(15) Spek, A. *Acta Crystallogr., Sect. D* **2009**, *65*, 148−155.

(16) Goodwin, H. A. *Top. Curr. Chem.* **2004**, *233*, 59−90.

(17) (a) Binnemans, K.; Jongen, L.; Bromant, C.; Hinz, D.; Meyer, G. *Inorg. Chem.* **2000**, *39*, 5938−5945. (b) Zhang, W.; Zhao, F.; Liu, T.; Yuan, M.; Wang, Z. M.; Gao, S. *Inorg. Chem.* **2007**, *46*, 2541−2555.

(18) Dorset, D. L. *Crystallography of the Polymethylene Chain: An Inquiry into the Structure of Waxes*; Oxford University Press: Oxford, NY, 2005.

(19) Akanni, M. S.; Okoh, E. K. *Thermochim. Acta* **1992**, *208*, 1−41.

(20) Marques, E. F.; Burrows, H. D.; da Miguel Graca, M. *J. Chem. Soc., Faraday Trans.* **1998**, *94*, 1729−1736.

(21) Gaspar, A. B.; Seredyuk, M. *Coord. Chem. Rev.* **2014**, *268*, 41−58.

(22) Tao, J.; Wei, R.-J.; Huang, R.-B.; Zheng, L.-S. *Chem. Soc. Rev.* **2012**, *41*, 703−737.

(23) (a) Hayami, S.; Karim, M. R.; Lee, Y. H. *Eur. J. Inorg. Chem.* **2013**, 683−696. (b) Hayami, S., Amphiphilic and Liquid Crystalline Spin-Crossover Complexes. In *Spin-Crossover Materials*; Halcrow, M. A., Ed.; John Wiley & Sons Ltd.: Chichester, 2013; pp 321−345.

(24) (a) Nagashima, H.; Inoue, H.; Yoshioka, N. *J. Phys. Chem. B* **2004**, *108*, 6144−6151. (b) Ghandi, M.; Zarezadeh, N.; Taheri, A. *Tetrahedron* **2010**, *66*, 8231−8237.

(25) Sheldrick, G. M. *Acta Crystallogr., Sect. A* **2008**, *64*, 112.